Heterogeneous corrosion of carbon steel used for casing in deep geological radioactive waste repository in contact with claystone

Annabelle Vernouillet, Delphine Neff, Eddy Foy, Valérie Maillot, Xavier Bourbon, Didier Crusset, Nicolas Michau, Franck Agostini, James Jay Dynes, Philippe Dillmann

Corrosion Science 241 (2024) 112472

Contents lists available at ScienceDirect

Corrosion Science

journal homepage: www.elsevier.com/locate/corsci

Heterogeneous corrosion of carbon steel used for casing in deep geological radioactive waste repository in contact with claystone

Annabelle Vernouillet [a,*], Delphine Neff [a], Eddy Foy [a], Valérie Maillot [b], Xavier Bourbon [b], Didier Crusset [b], Nicolas Michau [b], Franck Agostini [c], James Jay Dynes [d], Philippe Dillmann [a]

[a] LAPA-IRAMAT, NIMBE, CEA, CNRS, Université Paris-Saclay, CEA Saclay 91191, Gif-sur-Yvette Cedex, France
[b] Andra, Research & Scientific Division, 1/7 rue Jean Monnet, Châtenay-Malabry Cedex 92298, France
[c] University of Lille, CNRS, Centrale Lille, UMR9013, LaMcube, Lille 59000, France
[d] Canadian Light Source, 44 Innovation Boulevard, Saskatoon, SK S7N 2V3, Canada

ARTICLE INFO

Keywords:
Deep geological disposal
Iron corrosion
Phyllosilicates
Claystone

ABSTRACT

The corrosion of C-steel in contact with the Cox claystone was studied under aerated conditions at 50°C, for 7 years, in a simplified laboratory experiment. A multi-scale and multi-technique approach, including SEM-EDX, Raman spectroscopy and STXM, was used to determine the nature and structure of the corrosion products and to better understand the mechanisms involved in the observed degradation. The effects of temperature, oxygen supply and the local influence of the composition and density of the claystone were examined here.

1. Introduction

Deep geological repository is considered by several countries as the reference solution to isolate high and intermediate long-lived radioactive waste, for as long as they are dangerous for humankind and the environment (over 100 000 years) [1]. In France, a multi-barrier system was designed to confine radionuclides [2,3]. High level radioactive waste is calcinated and vitrified before being put in a stainless steel container enclosed in a carbon-steel overpack. The waste packages will then be placed in a horizontal micro-tunnel equipped with a carbon steel casing. The host rock, the Callovo-Oxfordian (Cox) claystone, at a depth of 500 m at the border of the Meuse / Haute-Marne departments, was chosen for its low permeability, and stable physical and chemical properties [4,5], ensuring safe confinement properties over a long period of time.

In order to ensure the confinement of the radionuclides for over 100 000 years, the structural integrity of the multi-barrier system must be preserved. It is therefore crucial to evaluate the degradation of carbon steel in contact with the Callovo-Oxfordian host rock with time and to understand the corrosion mechanisms involved. Several environmental factors can influence the severity and the nature of the corrosion such as the presence of oxygen and the temperature. These factors vary during the first few years of corrosion. Indeed, once filled with waste packages, the aerated tunnels will be sealed. Several studies show that the amount of oxygen in the tunnels will then decrease over time, leading to an anoxic environment [6–10]. Moreover, due to the radioactivity, the initial temperature of the waste packages will range from 50°C to 100°C [11] depending on the exothermicity of the nuclear waste. The feasibility of the multi-barrier system is tested in an underground research laboratory (URL) that was built by the French National Radioactive Waste Management Agency (Andra) as part of the Cigéo project (Industrial centre for geological disposal). That is why different corrosion systems must be studied, representative of these different environments and their evolution from the initial aerated conditions with 50–100°C temperatures at the beginning of the storage, to the anoxic conditions latter.

In situ and laboratory experiments as well as the study of archaeological analogues all show that, at ambient temperature, the long term corrosion of carbon-steel in contact with claystone in aerated conditions mainly leads to the formation of goethite (α-FeOOH) and/or lepidocrocite (γ-FeOOH) [12–16]. A mixture of maghemite (γ-Fe_2O_3) and magnetite (Fe_3O_4) can also be found, embedded in the oxyhydroxide matrix [12,15,16]. To our knowledge the only studies on the corrosion of carbon steel in contact with claystone at slightly higher temperatures (85°C or 90°C) have been carried out under anaerobic conditions [17–22]. On the contrary, to our knowledge no study examined the corrosion of low alloy steel in clay between 50 °C and 90°C, in aerated conditions.

* Corresponding author.
E-mail address: annabelle.vernouillet@cea.fr (A. Vernouillet).

https://doi.org/10.1016/j.corsci.2024.112472
Received 29 April 2024; Received in revised form 29 July 2024; Accepted 18 September 2024
Available online 19 September 2024

The experimental setup considered in the present paper, initially designed for mechanical studies [23], offers the unique opportunity to study 7 year old low carbon steel corroded samples in an aerated clayey environment at 50°C. This multi-technique and multi-scale characterisation study aims to better understand the degradation mechanisms during the first years of deep geological disposal, *i.e.* aerated corrosion of carbon-steel in contact with claystone and to examine the possible effect of the temperature, oxygen supply but also possible local influence of the composition and density of the claystone.

2. Materials and method

The samples studied is this article came from an experimental set-up at the LaMcube laboratory in Centrale Lille Institut (France). It was designed in collaboration with Andra to study the deformation induced by the formation of the corrosion products. This specific topic has already been studied for reinforced concrete, by Chen *et al.* [24].

The carbon steel used in this experiment was E24. The composition in weight percent is presented in Table 1.

The Callovo-Oxfordian claystone was taken from the Bure URL. Its mineralogical weight composition at 495 m deep is given in Table 2. Its elemental weight composition was measured by EDX on each of the four samples studied here (Table 3).

The electrolyte was constituted of water at 40 mmol/L of NaCl. Its pH, measured at 21°C, was 8.26.

In order to accurately measure the macroscopic volume expansion caused by the corrosion, the number of metal/clay interfaces were multiplied. The experimental set-up was therefore composed of a stacking of 7 Cox-claystone cylinders of 58 mm of diameter and 12 mm of thickness (Fig. 1). Each interface between claystone cylinders contained a carbon-steel coupon of 40 mm of diameter and 2 mm thickness. To maintain the whole stack upright, it was placed in siliceous sand and in a sintered stainless steel cylinder. The frame was immersed in the electrolyte which was heated at 50°C for the first 5 years of the experiment. For the last two years, the electrolyte was maintained at room temperature. Two stacks of carbon-steel/claystone (1 and 2) were placed in the same container filled with 150 L of solution and therefore corroded under identical conditions. As the electrolyte was heated at 50°C, some evaporation occurred. However, a vapour trap limited the amount of water loss. Moreover, a sensor was placed at the top of the vertical holder in order to detect the water level: if needed water was added. Thanks to these precautions, the water level was always 20 to 30 cm above the top of the stacks.

After 7 years, the experimental set-up was dismantled. Both stacks were taken out of the electrolyte and out of the sand before being rinsed with the electrolyte. They were then mounted in epoxy resin and scanned by X-ray tomography to locate the metal samples within the claystone. The stacks were then sliced in between the carbon-steel samples and mounted again in epoxy resin. Two samples from each stack were then characterised to determine the nature of the corrosion products formed. The samples were cut in half to analyse the cross-section, grinded on SiC paper and then polished using 1 μm diamond particles under ethanol.

The samples were analysed using X-ray tomography, optical and electronical microscopy, Raman spectroscopy and X-ray diffraction.

The tomography setup used was the one of the experimental platform ISIS4D X-ray CT platform in Lille university (www.isis4d.univ-lille.fr). Due to the sample sizes, the voxel size is 60 μm. This did not allow analysis of the corrosion product layers, but a full sample scale view (location of the steel sample and cracks).

Table 1
Weight composition of the E24 - carbon steel [25].

Elements	C	Mn	P	N	S	Fe
Weight %	0.17	1.40	0.045	0.009	0.045	Bal.

Table 2
Mineralogical composition of the Cox claystone at a depth of 495 m depth [5,26].

Mineral	Amount (wt%)
Illite	16
Kaolinite	3
Chlorite	2.2
K-Feldspar	2
Quartz	22
Calcite	21
Dolomite	3
Pyrite	0.7
Titanium minerals	0.3
Siderite	1.9
Phosphate minerals	0.3
Plagioclases	1

The optical microscope (OM) was an Imager A2 Axio Zeiss coupled with an AxioCam 305 camera. The plate was controlled by ZenCore 3.3 software.

The SEM observations were performed using a Jeol 7100 F field effect scanning electron microscope in backscattered electron mode using a probe current of 10–12 nA with a 15 kV acceleration voltage. EDX analyses were performed with a silicon drift detector. To avoid charge accumulation, the samples were coated with a carbon-layer of approximately 20 nm thick.

The cross-sections were studied by identifying the corrosion products (CP) and the transformed medium (TM). The transformed medium is defined as a transition zone between the corrosion product layer (CPL) and the rock, containing elements coming from the claystone (silicon and calcium) in addition to iron coming from the metal. As there is 2.3 ± 1.5 wt% of iron in the claystone, the TM/soil interface corresponds to an iron concentration lower than 3 wt%. The CP layer thickness was measured every 100 μm all around the samples.

Two Raman spectrometers were used to identify the nature of the corrosion products: an INvia Reflex from Renishaw equipped with a 532 nm-wavelength laser with a CCD detector. A lead glass filter was used to reduce the intensity received by the sample around 10–100 μW. In order to focus the laser on regions of interest a 50x objective from a LEICA microscope was used. The laser beam size on the sample was approximately 1 μm and the spectral resolution used was 2 cm^{-1}. The other microscope used (at the MONARIS laboratory, Paris, France) was a Senterra from Brucker equipped with a 785 nm wavelength laser and an Olympus 50x IR long distance objective. The analysed area had a diameter of 3 μm. The spectral resolution was 4 cm^{-1}.

Scanning transmission X-ray microscopy (STXM) characterisations were performed at the Canadian Light Source (CLS), University of Saskatchewan (Canada) on the SM 10ID-1 beamline to provide spatial information on the nanostructure and the chemical environment of the Si in iron phyllosilicates in areas of interest previously identified by SEM-EDX. Si K-edge (1830–1880 eV) raster scanned images (100−200) were collected at a spatial resolution of 30 nm (beam flux 10^8 photons/s) on thin foils cut perpendicular to the surface using an electron ion-beam double column microscope (SEM-FIB). The microscope used was a FEI Helios Nanolab 660 from CIMAP/GANIL in Caen, France. The acceleration voltage ranged from 0.5 kV to 30 k and the ion current from 1 pA and 65 nA. Platinum was deposited on the surface of the area of interest using the electron and ion beams to protect from irradiation and ensure the mechanical strength of the thin foil during thinning. Ga ions were used for the thinning of the foil which was flipped between each pass of the ion beam to avoid any mechanical stress. The thinning was performed until the thickness reached 1 μm for analysis at the Si K-edge. Principal component analysis was used to derive spectra from pixels with the same spectral signal. The energy scale of the derived spectra was calibrated using quartz at 1846.6 eV. The experimental data were decomposed using a least squares method with standard reference spectra, from our Si K edge database (Table 4), normalized to an

Table 3
Weight composition of the Cox claystone (measured by EDX on coupons of the present study).

	O	Na	Mg	Al	Si	P	S	Cl	K	Ca	Mn	Fe
Weight %	57.7	0.1	1.4	7.5	20.2	0.1	0.3	0.1	2.0	8.4	0	2.3
Uncertainty	5.8	0.2	0.1	0.6	2.6	0.1	0.2	0.1	0.5	3.2	0	1.5

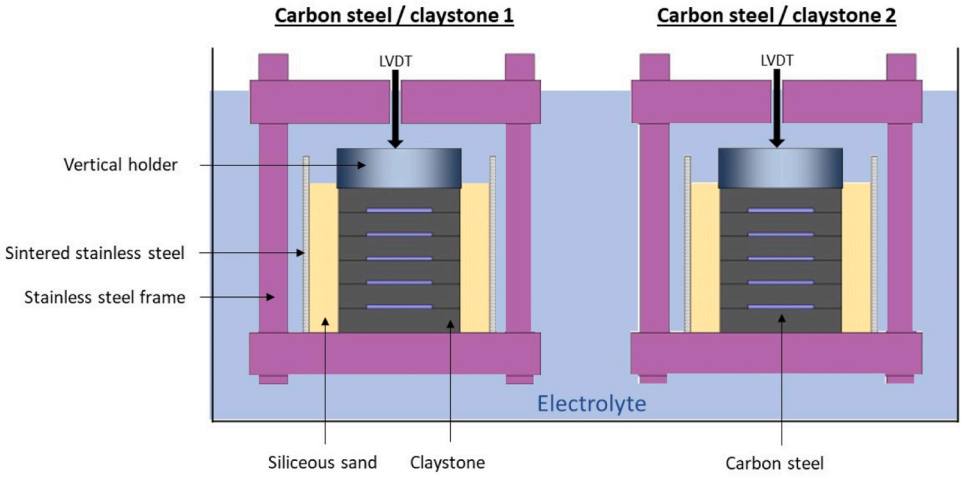

Fig. 1. Schematic of the experimental set-up at LaMcube, Centrale Lille showing both stacks in the same container, LVDT stands for linear variable differential transformer and is used to measure the displacement of the stack [27].

Table 4
Iron phyllosilicates references for STXM analyses see [28].

Group	Phyllosilicate	Composition
Serpentine	BerthierineGreenaliteCronstetite	$(Fe^{2+},Fe^{3+},Al,Mg)_{2-3}(Si,Al)_2O_5(OH)_4$ $(Fe^{2+},Fe^{3+})_{2-3}Si_2O_5(OH)_4$ $Fe_2^{2+},Fe^{3+}(Si,Fe^{3+})O_5(OH)_4$
Smectite	Nontronite Garfield[1]	$Na_{0.3}Fe_2^{3+}(Si,Al)_4O_{10}(OH)_2.n(H_2O)$
	Nontronite Nau−2[2]	
	Montmorillonite	$M_{0.97}^{+}(Si_{7.57}Al_{0.1}Fe0_{.42})(Al_{0.52}Fe_{3.32}Mg_{0.7})O_{20}(OH)_4$, M^{+}=Ca, Na, K
	Saponite	$(Ca_{0.12}Na_{0.32}K_{0.05})(Al_{3.01}Fe_{0.41}^{3+}Mg_{0.54})(Si_{7.98}Al_{0.02})O_{20}(OH)_4$ $Ca_{0.3}(Fe^{2+},Mg,Fe^{3+})_3(Si,Al)_4O_{10}(OH)_2\bullet 4(H_2O)$
	Kaolinite	$(Mg_{0.02}\ Ca_{0.01}Na_{0.01}K_{0.01})(Al_{3.86}Fe_{0.02}^{3+}\ Ti_{0.11})(Si_{3.83}Al_{0.17})O_{10}(OH)_8$

[1] Whitman County, Washington, USA
[2] Clay Source Repository of the Clay Minerals Society (Purdue University, West Lafayette, IN, USA)

absolute linear absorbance corresponding to a phase thickness of 1 nm (expressed in optical density).

A detailed description of the analysis method can be found in literature [28].

All thermodynamic calculations were done with the Geochemist's workbench package. The database used was the ThermoChimie_v10a developed by the consortium Andra-Ondraf/Niras-NWS [29–31].

3. Results

3.1. Global characterisation

The X-ray tomographies of the two stacks are presented in Fig. 2, along with two cross-sections. The two stacks did not present the same intensity of corrosion damage. Indeed, samples 1-F and 1-E were extensively corroded, especially on the first cross-section, whereas samples 2-F and 2-E did not present visible metal loss at this scale of observation. Moreover, for the first stack, the top samples seemed more corroded than the samples at the bottom: samples 1-F and 1-E were particularly damaged on both cross-sections whereas samples 1-C, 1-B and 1-A presented no detectable metal loss on the first cross-section.

Samples 1-E, 1-B, 2-E, 2-B were cross-sectioned for further analysis. Even though it is with a less importance, SEM images showed that the difference in the severity of the corrosion between top and bottom samples was also present in the second stack. Sample 2-E presented significant metal loss and corrosion product formation (Fig. 3.a) whereas for sample 2-B the metal loss seemed more homogeneous and significantly less important (Fig. 3.b).

From these comparisons, the following observations emerged:

- Samples from stack 1 were more corroded (metal loss observed on the tomography pictures) than samples from stack 2,
- In each stack, top samples presented a higher metal loss compared to the bottom samples (tomography and SEM observations).

3.2. Nature of the corrosion products: first stack

Samples 1-E and 1-B were characterised in order to identify the nature of the corrosion products formed on the samples of the first stack.

Sample 1-B (Fig. 4) was composed of a corrosion product layer and a transformed medium . The latter part was identified by the presence of elements coming from the claystone (silicon and calcium) in addition to iron coming from the metal. A large crack was visible in the middle of the CPL. The corrosion product layer was 6 μm thick with minimum of 1 μm and a maximum of 29 μm. The EDX mappings indicated that the corrosion products on sample 1-B were mainly composed of iron and oxygen (Fe 56 wt%, O 34 wt%) and of calcium, and oxygen (O 51 wt%, Ca 43 wt%, Fe 6 wt%). These CP were found all around the metal and were identified by Raman spectroscopy (not presented here) as made of goethite (FeOOH) and calcite ($CaCO_3$). Calcite was mostly located at the CP/TM interface but was also found mixed with the goethite. A non-continuous layer of an iron, sulphur and oxygen containing phase was

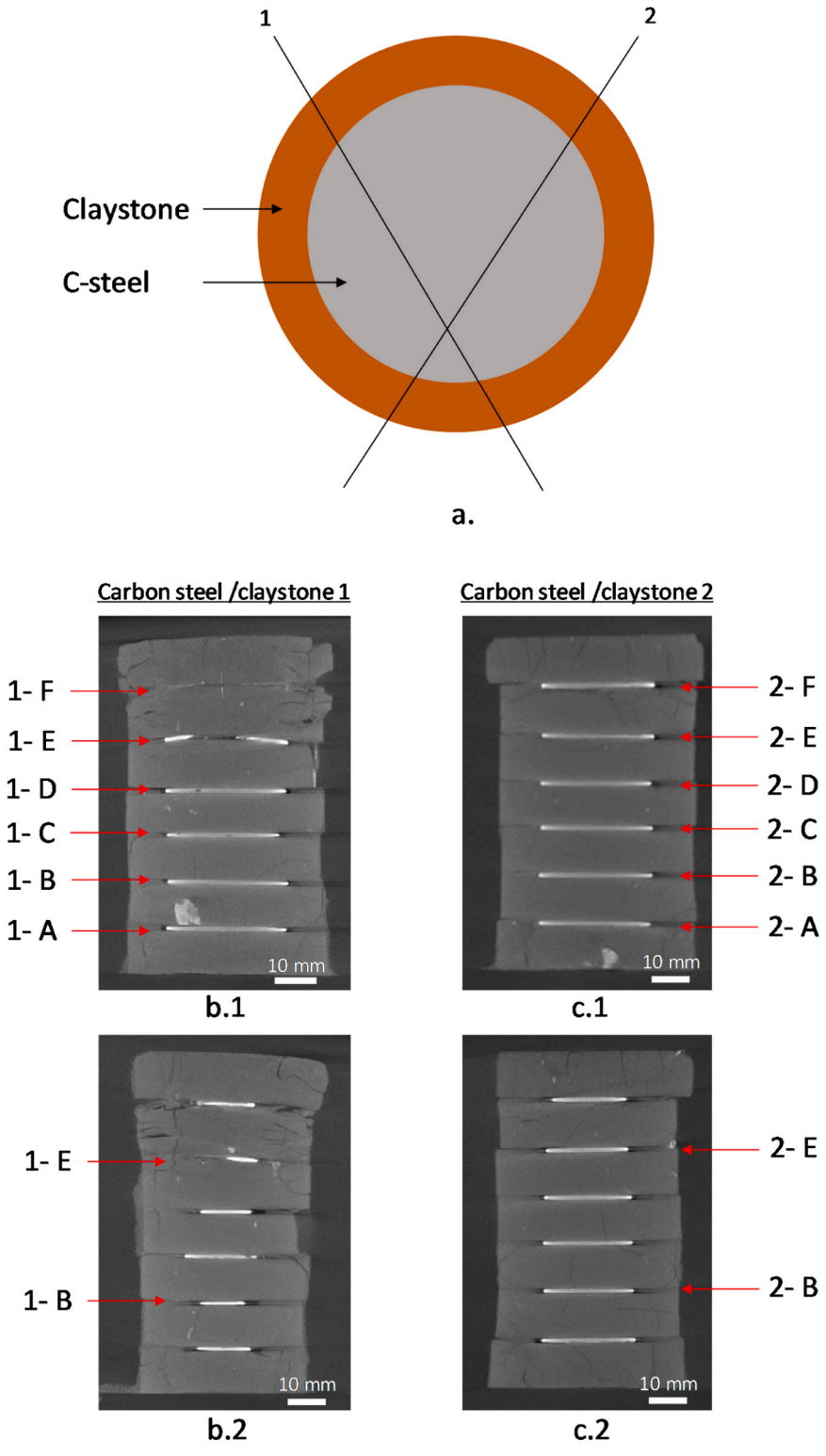

Fig. 2. Micro-tomography of the two carbon steel/claystone stacks. a. Schematic view from above of the stack with lines 1 and 2 representing the two tomography cross-sections, b.1 First stack, cross-Section 1, b.2 First stack, cross-Section 2, c.1 Second stack, cross-Section 1, c.2. Second stack, cross-Section 2.

also observed, primarily at the interface with the TM (Fig. 4). This sulphur containing phase could not be identified by Raman spectroscopy as no other Raman signatures apart from goethite and calcite were detected in the spectra acquired on this thin layer. Finally, chemical composition analyses suggested that a silicon rich phase (between 12 and 17 wt%) was present in two localised regions of the sample, within the CP layer (not shown on figure). At this location, no Raman spectra characteristic of iron-silicates could be identified, either because of high fluorescence phenomenon or because only goethite was detected.

All areas of sample 1-E that were analysed were composed of a corrosion product layer and a transformed medium (Fig. 6.a, Fig. 7.a and Fig. 9). The TM was identified by the presence of silicon, calcium and iron. However, the corrosion of sample 1-E was extremely heterogeneous. Most of the cross section presented a continuous corrosion

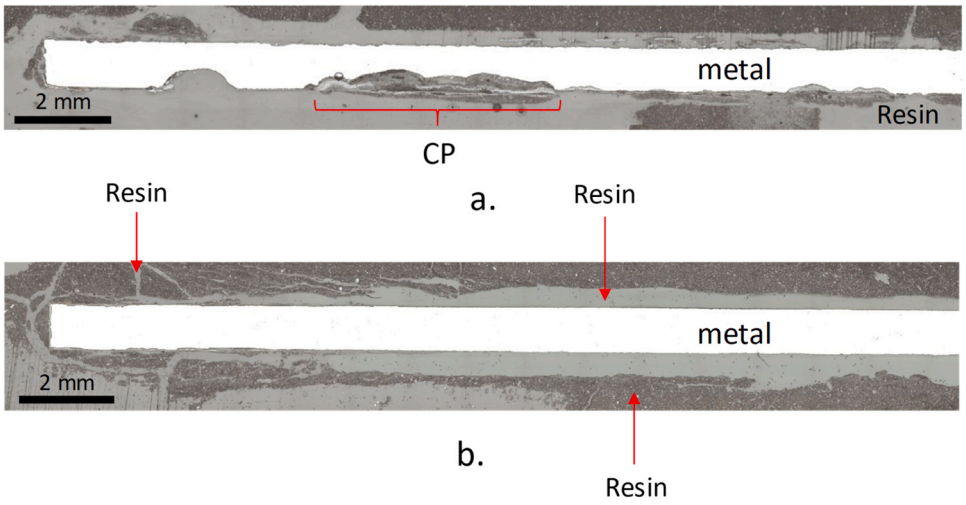

Fig. 3. a. OM image of sample 2-E, b.OM image of sample 2-B. Both samples were mounted twice in resin, therefore both resins (dark and light grey) are visible on the OM cross-section.

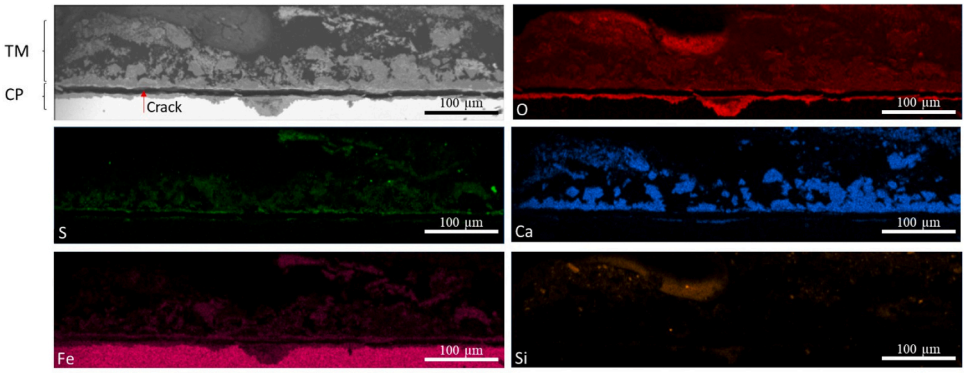

Fig. 4. SEM image and EDX mappings of the 1-B sample.

products layer (Fig. 5.b, zone 1) on the remaining metallic substrate. In several areas the sample presented significant corrosion of the metal with a full loss of metal (Fig. 5.c), the middle part of the sample was completely corroded). Very few CP were present in this area but were located along the original surface of the sample. Most of the metal was probably in the transformed medium as iron was detected by EDX at 5 mm from the original metal sample. On the SEM image Fig. 5.c, zone 3, on the right handside, the steel sample is fully corroded.

Analysis of zone 1 revealed the following phases: calcite (Ca and O detected), an iron sulphur and an iron and oxygen rich phase at the CP/TM interface (Fig. 6.a). Goethite was the main corrosion product and was located at the interface with the metal. The sulphur rich phase was identified by Raman spectroscopy (Fig. 6.b) as a mix of mackinawite (298 cm^{-1}), partially oxidised mackinawite (319 cm^{-1}) and greigite (352 and 361 cm^{-1}). Greigite is a mix of Fe II and Fe III ($Fe^{2+}Fe_2^{3+}S_4$) and mackinawite (FeS_{1-x}) is a Fe II sulphide but can contain up to 20 % of Fe III [32,33]. The same type of spectra, main peak at 298 cm^{-1} and smaller peaks at 208, 259, 356 and 387 cm^{-1}, was obtained by Bourdoiseau *et al.* for aged synthesised mackinawite [32]. The authors confirmed the identification of this phase with XRD analyses. Langumier

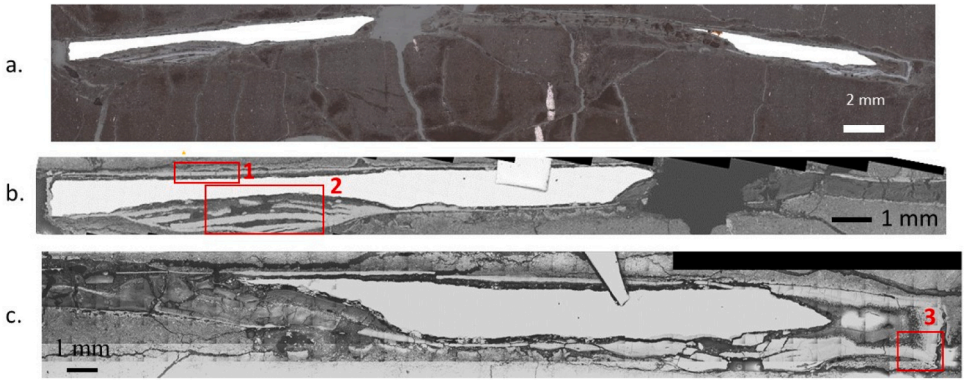

Fig. 5. Sample 1-E, a. OM image of sample 1-E, b. SEM image (BSE) of the left hand-side of a., c. SEM image (BSE) of the right-hand side of a.

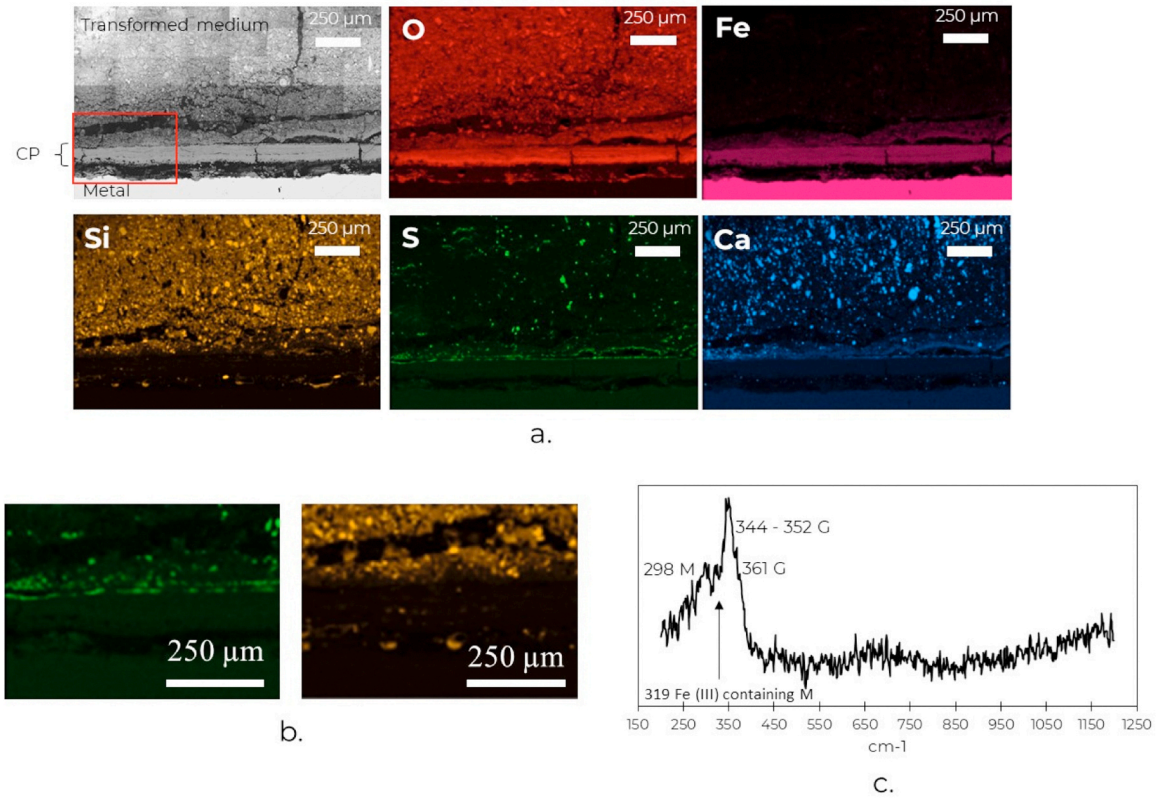

Fig. 6. Sample 1-E, a. SEM image and EDX mappings of Zone 1 (Fig. 5), b. Zoom of the red rectangle on SEM image, c. Raman spectrum of the sulphur, iron and oxygen rich phase at the CP/TM interface of sample 1-E, G: greigite, M: mackinawite.

et al. [34] showed that the Raman signature of synthetic partially oxidised mackinawite are bands at 318 cm^{-1} and 354 cm^{-1}. This identification was also confirmed by XRD analyses. Bourdoiseau *et al.* also identified partially oxidised mackinawite with the following Raman bands [32]: main peaks at 255, 311 and 322 cm^{-1} and smaller peaks at 125 and 175 cm^{-1}. Synthetic greigite was identified by Bourdoiseau *et al.* by Raman bands at 350 and 360 cm^{-1} [35] and natural greigite within a rust layer on a historical sample was identified at 350 and 365 cm^{-1} [36]. The identification was in both cases confirmed by XRD analyses. It is probable that the oxygen detected by EDX at this location is due to the surrounding phases.

The corrosion products in zone 2 had a lamellar layout (Fig. 7.a.). These lamellae were exclusively composed of goethite (Fig. 8). Their density seemed to decrease the closer they were to the metal (Fig. 7.b.). Moreover, Raman spectroscopy showed that the goethite was less crystallised when closer to the metal. Indeed, the Raman signal of goethite for points 2 and 3 (Fig. 8) was less intense, noisier and the Raman bands were less defined than for point 1. The density in a lamella was also heterogeneous and seemed to be lower in the part closer to the metal. At the CP/TM interface calcite (identified by Raman spectroscopy, spectrum not showed here) and an iron, sulphur and oxygen rich phase (Fe 60 wt%, S 22 wt%, O 18 wt%) were detected.

EDX mappings (Fig. 9) and Raman spectroscopy (not shown here) of region 3 indicated that the nature of the corrosion products was the same as for regions 1 and 2. Moreover, for these regions, the goethite layer was also less dense at the metal/CP interface than in the rest of the layer.

Whatever the region of interest studied, the nature of the corrosion products on sample 1-E was the same: calcite, thin layer of iron sulphide and goethite. The organisation of these CP was similar as well: calcite and iron sulphide were systematically localised at the CP/TM interface whereas goethite was always at metal/CP interface.

3.3. Nature of the corrosion products: second stack

The two samples studied on the second stack were in the same position as the ones on the first stack: 2-B and 2-E.

The corroded sample 2-B (Fig. 10) was composed of a scale of corrosion products and a transformed medium (TM). The latter part was identified by the presence of elements coming from the claystone (silicon and calcium) and from the metal (iron). The average thickness of the corrosion product layer was of 19 µm with a minimum of 4 µm and a maximum of 169 µm. The SEM and Raman spectroscopy analyses of sample 2-B showed a predominance of goethite as well as calcite and mackinawite at the CP/TM interface (Fig. 10, Fig. 11.a.). In addition, the EDX mappings also revealed the presence of silicon, iron, and oxygen rich phase in the internal corrosion product layer, in addition to goethite. This phase was located either close to the CP/metal interface or at the interface with mackinawite. Its composition measured by EDX was approximately Si 19 %wt, O 40 %wt, Fe 41 %wt and was observed on 75 % of the surface on the studied cross-section. Similar compositions were detected by Schlegel *et al.* after anoxic corrosion in contact with claystone, at 90°C and identified by XRD and Si-K edge XANES as a mix of iron phyllosilicates [37,38]. This iron-silicate was analysed by Raman spectroscopy at 532 nm and 785 nm. No signal was obtained at 532 nm. However, one spectrum acquired with the 785 nm laser had a low signal to noise ratio, suggesting that this phase was poorly crystalline (Fig. 11. b) and particularly fragile under the laser beam. Despite the presence of bands at 212 cm^{-1}, 409 cm^{-1}, 554 cm^{-1}, and 1360 cm^{-1}, no precise identification was possible. The band at 212 cm^{-1} can be attributed to the O-H-O vibrational mode in the serpentine group minerals [39] and the bands between 540 cm^{-1} and 590 cm^{-1} were attributed to the bending of the Si-O-Si in alkali silicate glass. However, the bands at 409 and 1360 cm^{-1} were not attributed to any vibration mode.

STXM characterisations (Fig. 12) were performed on a silicon-rich area (Fe 37 wt%, O 44 wt%, Si 18 wt%). The experimental data was

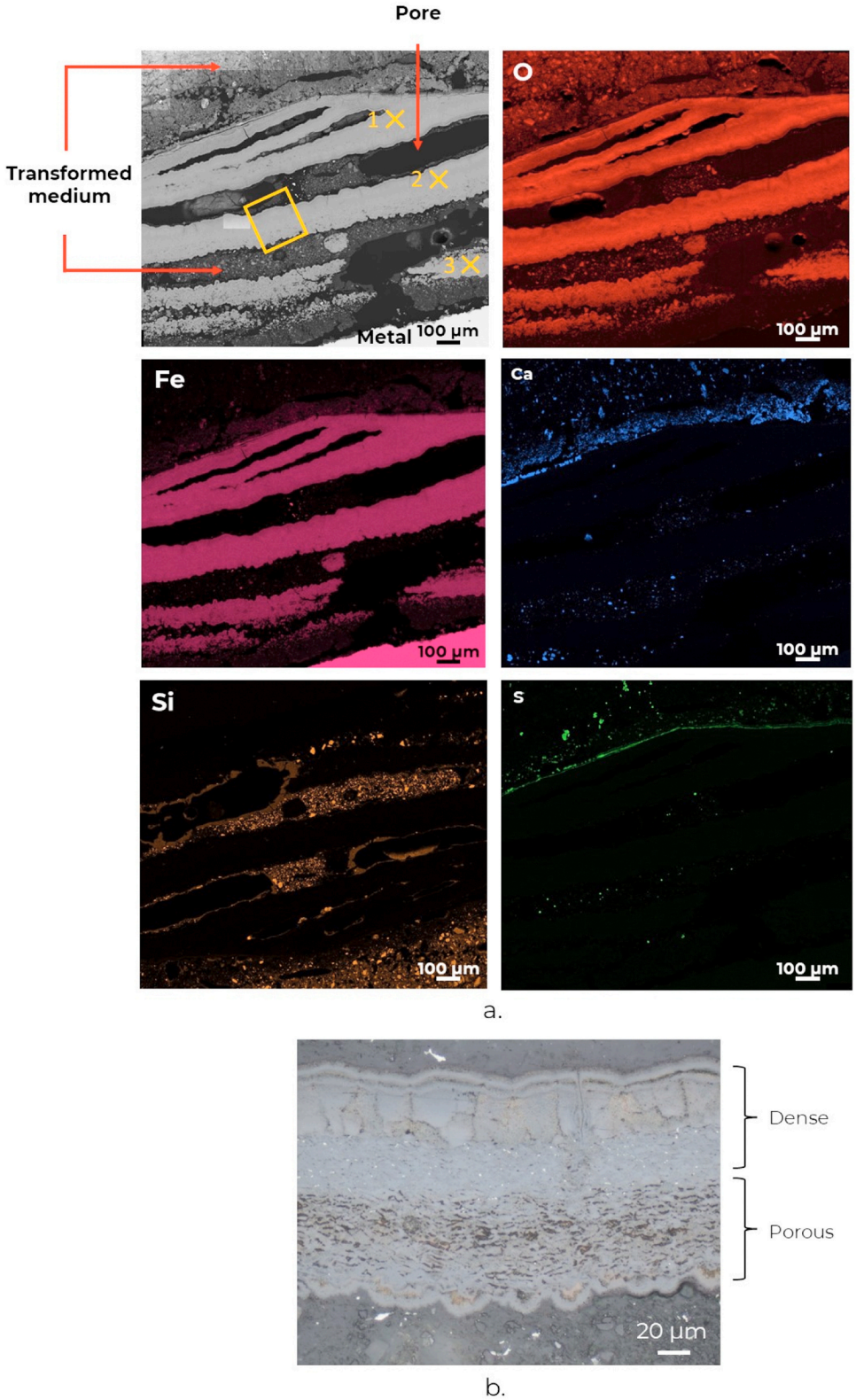

Fig. 7. Sample 1-E, a. SEM image and EDX mappings of the zone 2 (Fig. 5.b), b. OM image of the yellow square on SEM image a.

analysed by comparing the obtained spectral signal to the one of references of the serpentine and smectite groups. The best fit, determined by considering the highest coefficient of determination and lowest chi-squared as well as global similarity of experimental and modelled spectra, was obtained for a mix of greenalite (65 wt%) and nontronite NAu-2 (35 wt%), see Table 4 for composition. This confirms the presence of a serpentine (greenalite) suggested by Raman spectroscopy in addition to the one of smectite. It is therefore probable that the iron phyllosilicates observed on sample 2-B were a mix of serpentine and smectite.

Sample 2-E presented significant corrosion compared to sample 2-B (Fig. 3). However, compared to sample 1-E, sample 2-E presented

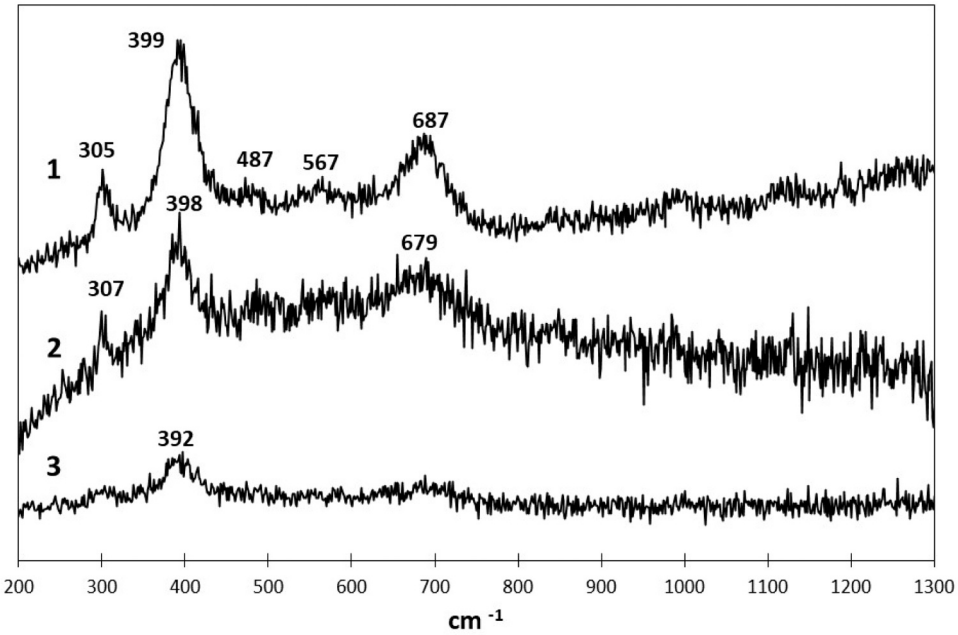

Fig. 8. Raman spectra of points 1, 2 and 3 on Fig. 7.a, sample 1-E.

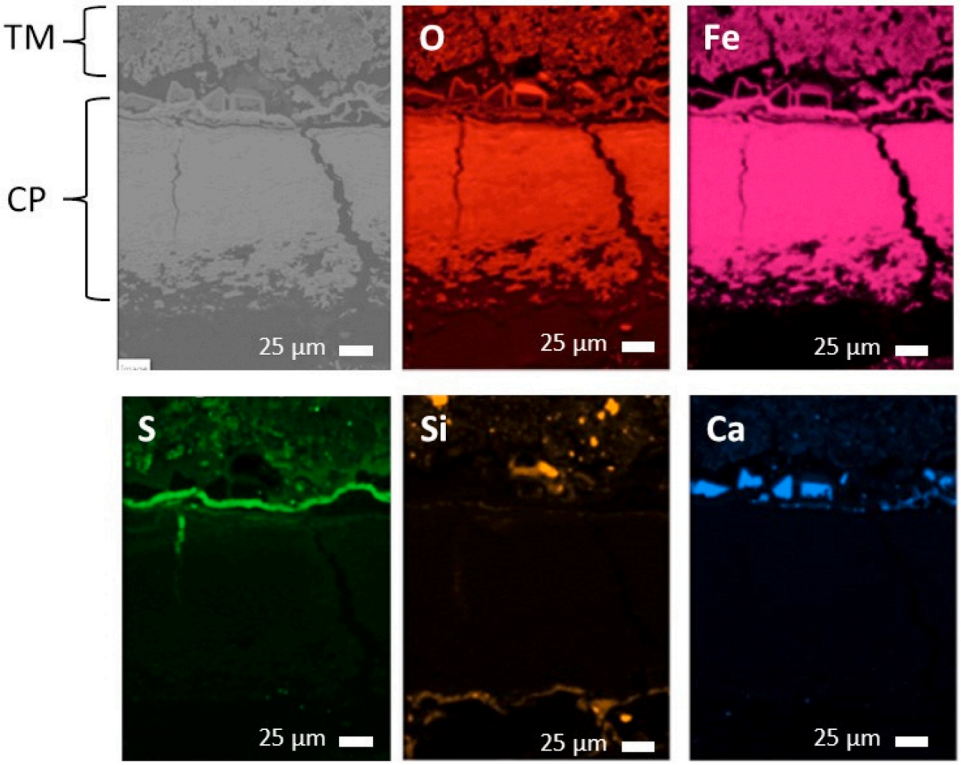

Fig. 9. SEM-BSE image and EDX mappings of zone 3 Fig. 5.c, sample 1-E.

significantly less corrosion damage. The layout was composed of a corrosion product layer and a transformed medium (Fig. 13). The TM was identified by the presence of silicon, calcium and iron. The corrosion product layer was of 52 µm with a minimum of 8 µm and a maximum of 205 µm, underlining its strong heterogeneity in thickness. Goethite, mixed with ferrihydrite were the main corrosion products (Fig. 13 and Fig. 14.a) and calcite and a sulphur rich phase were detected at the CP/TM interface. As for sample 2-B, the sulphur rich phase was identified by Raman as mackinawite [32] (Fig. 14.a, peak at 304 cm^{-1}). A silicon-iron-oxygen phase was observed within the internal corrosion layer in addition to goethite both close to the interface with the metal and in contact with the mackinawite. The Raman spectra, obtained at 785 nm, suggested that this phase is amorphous or poorly crystalline. The main Raman bands, for all six spectra are at 223 cm^{-1}, 295 cm^{-1}, 542 cm^{-1} and 1350 cm^{-1} which were similar to the bands observed on sample 2-B. The iron-silicates on both samples were therefore probably of the same nature. Two Raman spectra also show bands at 127, 134 and 285 cm^{-1}. Finally, one spectrum showed a band

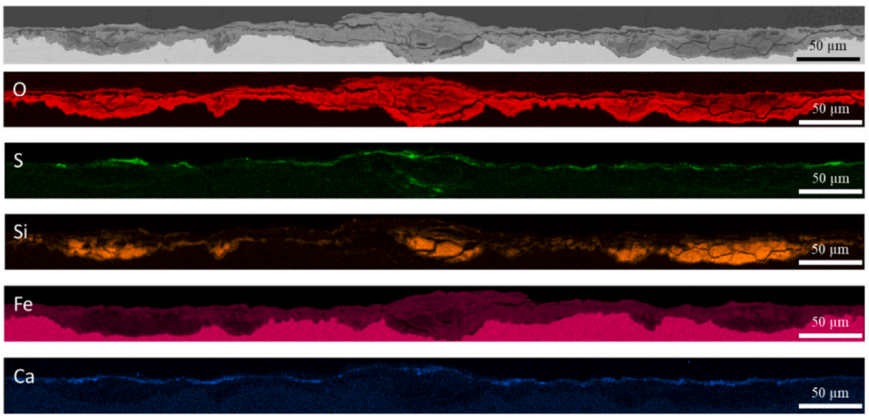

Fig. 10. SEM image and EDX mappings of an analysed region of sample 2-B.

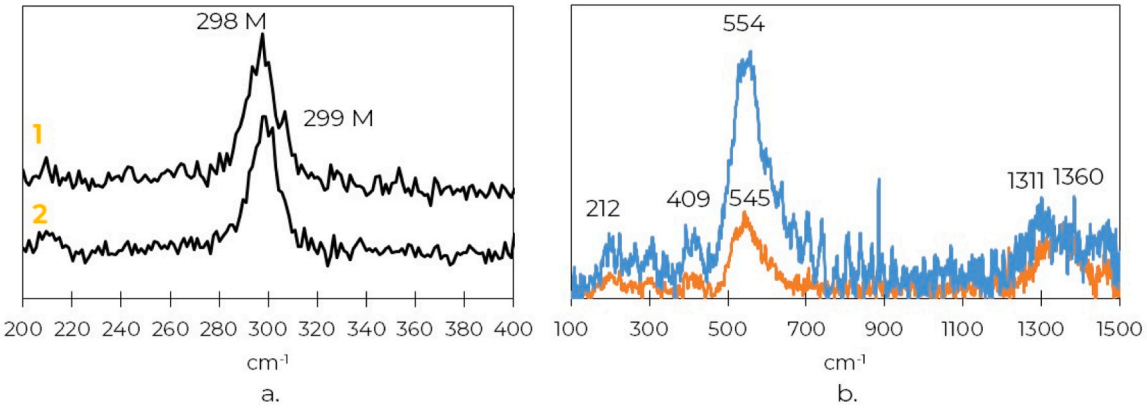

Fig. 11. Raman spectra of the a. sulphur rich phase at 532 nm, M: mackinawite and b. silicium-iron-oxygen phase at 785 nm on sample 2-B.

at 1160 cm^{-1}. Ishii et al. attributed bands at 127 and 130 and 285 cm^{-1} to the vibrational modes of the hexagonal Si_2O_5 lattice of a serpentine [40]. Bands between 278 and 310 cm^{-1} could also be attributed the vibrational mode of the δ (Si-O-Si) of a smectite [41]. The band at 1160 cm^{-1} could be attributed to the anti-symmetrical stretching of the Si-O_{nb} bond for 1:1 phyllosilicates [42] and A_1 (ν_1) Si-O_b mode for the 2:1 mineral group [43]. The bands around 1300 cm^{-1} were not attributed to any vibrational modes. From this analysis, it is not possible to discriminate between serpentine or smectite.

STXM characterisations (Fig. 15) were performed on a silicon-rich area. The experimental data was analysed by comparing the experimental spectral signal to the one of reference of the serpentine and smectite groups. The best fit, determined by considering the highest coefficient of determination and lowest chi-squared as well as general aspect of the spectra, was obtained for a mix of nontronite Garfield (89 wt%) and amorphous glass (11 wt%) for zone 1 and greenalite (70 wt%) and nontronite NAu-2 (30 wt%) for zone 2 (see Table 4 for the compositions of the phyllosilicates and the differences between each nontronite). These analyses are in agreement with the Raman spectroscopy characterisation which showed a possible mix of serpentine and smectite.

The nature and organisation of the CP are summarised Fig. 16.

4. Discussion

This first part of the discussion focuses on the differences observed in the severity of the corrosion according to the vertical position of the samples on both stacks. Considering the general morphology of the samples, X-ray tomography, OM and SEM observations showed that samples located at the top were significantly more corroded than samples at the bottom. There seems to be a correlation between the position of the sample in the stack and the corrosion rate. As the experimental set-up ensured that the level of water remained 20 to 30 cm above the stacks at all times, the highest corrosion activity observed for the top samples is not the result of drying/humidification cycles that could have caused important oxygen supply to the reactive interface.

The amount of oxygen initially present in the 150 L container was calculated at 0.028 mol (neglecting the water addition), considering the equilibrium between the dissolved and gaseous oxygen at 50°C [44]. The tomography of the first stacks (Fig. 2) indicated that the coupons 1-E and 1-F are the samples with the higher mass loss. The coupon 1-F seems to be almost completely transformed into corrosion products. The quantity of oxygen to corrode entirely the metal constitutive of a coupon is evaluated as follows. The main anodic reaction considered for the corrosion of the metal is $Fe \rightarrow Fe^{2+} + 2e^-$ and, as the environment is aerated, the cathodic reaction $H_2O + \frac{1}{2}O_2 + 2e^- \rightarrow 2OH^-$. The amount of oxygen needed to completely corrode coupon 1-F is 2.2 mol. Considering these calculations, the dissolved oxygen present initially in the tank is therefore not sufficient to account for the corrosion observed on all samples. If the consumption of oxygen by the corrosion process is sufficiently fast, the amount of oxygen available at the reactive interface is therefore controlled by transport phenomena and consequently different at the top and the bottom of the stack. The oxygen diffuses from the atmosphere/water interface located at the top of the setup, corroding the top samples first. With time the metal of the top samples is progressively oxidised. This process slows down progressively with the growth of the corrosion layers on these samples leading to a decrease of the oxygen consumption by the top part on both stacks. As the renewal of oxygen in the solution is constant, it therefore can diffuse deeper in

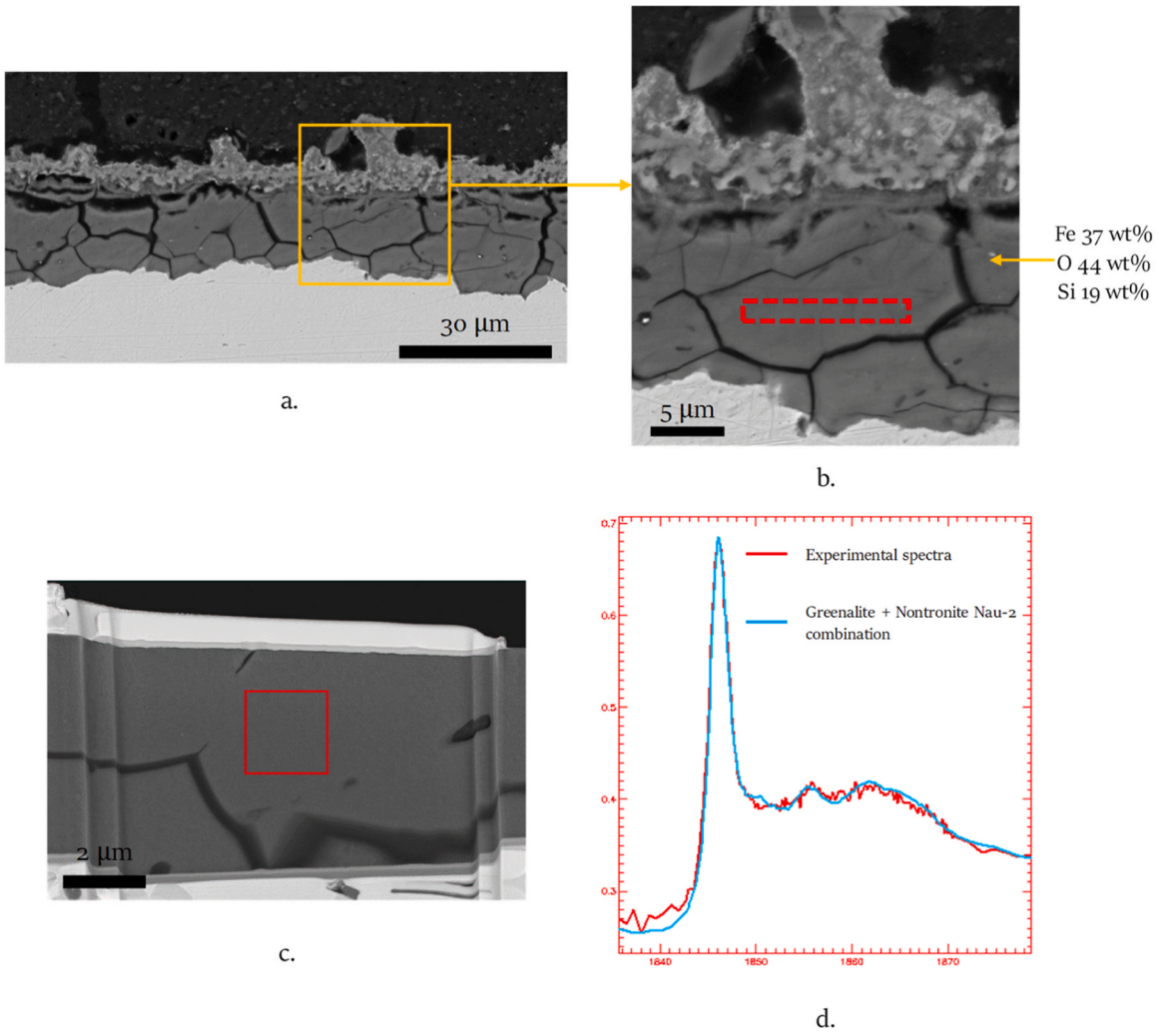

Fig. 12. Sample 2-B, a. SEM-BSE image of the area of interest for STXM characterisation, b. Zoom of the yellow square on a., the red rectangle marks the location of the thin foil, c. Thin foil, d. Experimental data obtained on the red square of c and linear combination fit (r^2= 0.989, chi^2=0.0186).

the experimental setup and interact with lower samples.

Comparing the samples at an equivalent depth in both stacks, it was also observed a difference of the intensity of corrosion between the top samples of the two stacks. Sample 1-E located at the top of the stack 1 is significantly more corroded than sample 2-E of stack 2 (parts of sample 1-E were completely corroded, Fig. 5). This can also be explained by a difference of oxygen supply between the two stacks. Indeed, the clay of stack 1 is much more cracked than the clay of stack 2 (see tomography on Fig. 2), highlighting the role of the transport properties. Cracks promoted diffusion shortcuts for oxygen that could have reached the metal more rapidly and in more important quantities, leading to more severe corrosion. It is not excluded that the precipitation of lower density corrosion products initiated new cracks, accelerating the process. For sample 1-E, this phenomenon of local oxygen supply could also have initiated a differential aeration effect, leading to a significant corrosion of anodic deaerated zones compared to more cathodic aerated ones explaining the particularly severe corrosion of some parts of the sample (Fig. 5, zone 2 and 3). On the contrary, for stack 2, for which clay appears to be less cracked, diffusion of oxygen from the outside water through the clay should be more difficult than for stack 1.

After these general considerations showing the influence of the geometry of the experimental set-up and of the density of the claystone, the corrosion layers were considered at a micrometric scale to understand their conditions of formation. First the formation of the iron sulphide phases is discussed. A thin layer of iron-sulphur-rich phases was observed on all four samples at the CPL/TM interface. Mackinawite, partially oxidised mackinawite and greigite were observed on sample 1-E, while only mackinawite was found on samples 2-E and 2-B. An iron sulphur rich phase was detected on sample 1-B but was not formally identified (no Raman signal detected).

The only sulphur source in the studied system was the pyrite from the embedding clay. Nevertheless, because of the aerated conditions, the formation mechanisms of the sulphides in the corrosion products must be discussed. Let us first consider their location. On sample 1-B it was clear that the sulphide phases precipitated along the original surface of the metal (Fig. 17), and for sample 1-E, zone 1, they were only present on the outer part of the corrosion products (outer lamella - Fig. 7). Both observations on the location, and especially the fact that the sulphide morphology reproduced the original shape of the coupon 1B, suggested that the sulphide phases formed at the beginning of the corrosion process, on the bare metal surface.

The presence of sulphides is an unexpected observation for an aerated environment. Literature data showing similar presence of iron sulphide on the metal is briefly reviewed here. This type of facies was observed in several experimental configurations both deaerated and aerated:

- Necib *et al.* also observed the presence of iron sulphide at the original surface location on 7-year old experiments in anoxic conditions (two years at ambient temperature then 90°C) [14]. The formation of

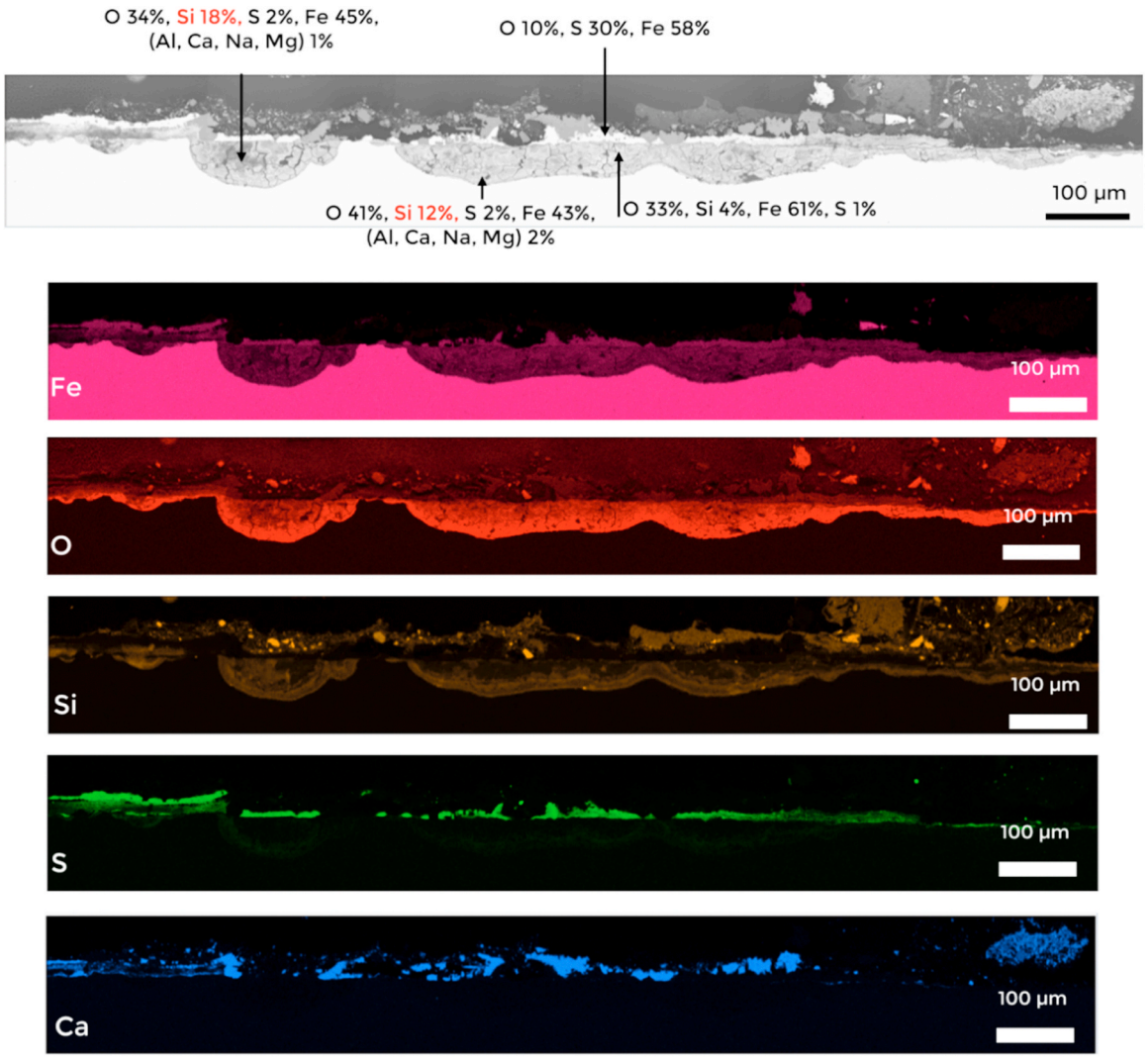

Fig. 13. SEM image (BSE) and EDX mappings of a region of interest on sample 2-E.

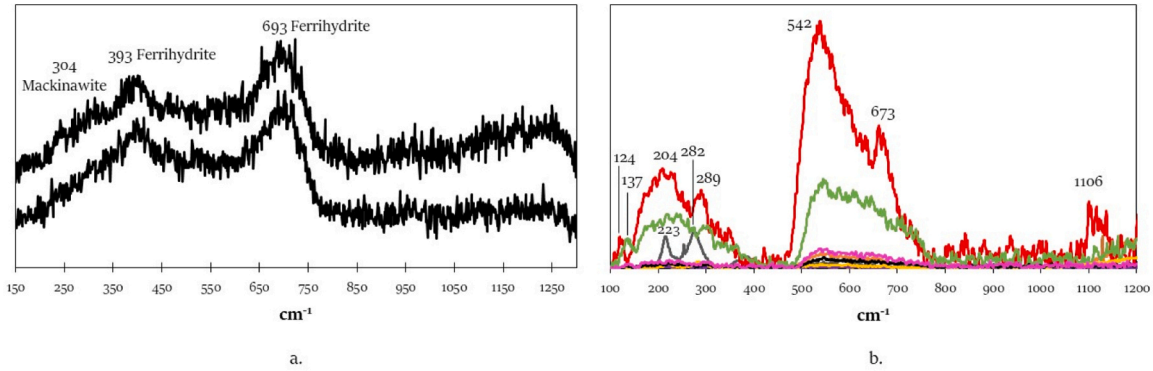

Fig. 14. Raman spectra of the a. sulphur rich phase at 532 nm and b. silicon-iron-oxygen phase at 785 nm, sample 2-E.

sulphides was explained in this study by the presence of sulphate reducing bacteria.

- The precipitation of iron sulphide was also observed by Schlegel *et al.* on carbon steel coupons corroded in a Cox argillite block in laboratory experiments conducted at 90°C under anoxic conditions. The dissolution of pyrite from the Cox was observed in this study thanks to backscattered electronic microscopy images showing a dissolved pyrite grain in Cox argillite in anoxic conditions [21]. The authors proposed in these conditions the direct dissolution of pyrite following the equation: $FeS_2 + H_2 \rightarrow Fe^{2+} + 2HS^-$
- Robineau *et al.* performed analyses of coupons corroded in a cementitious low pH grout in aerated conditions at 80°C, for 30 days. They explained the provenance of sulphide ions in the solution by the presence of pyrite in the composition of the grout [45]. They proposed as an explanation that in such aerated thermodynamic conditions of the solution, temperature of 80°C and pH of 10 (at ambient

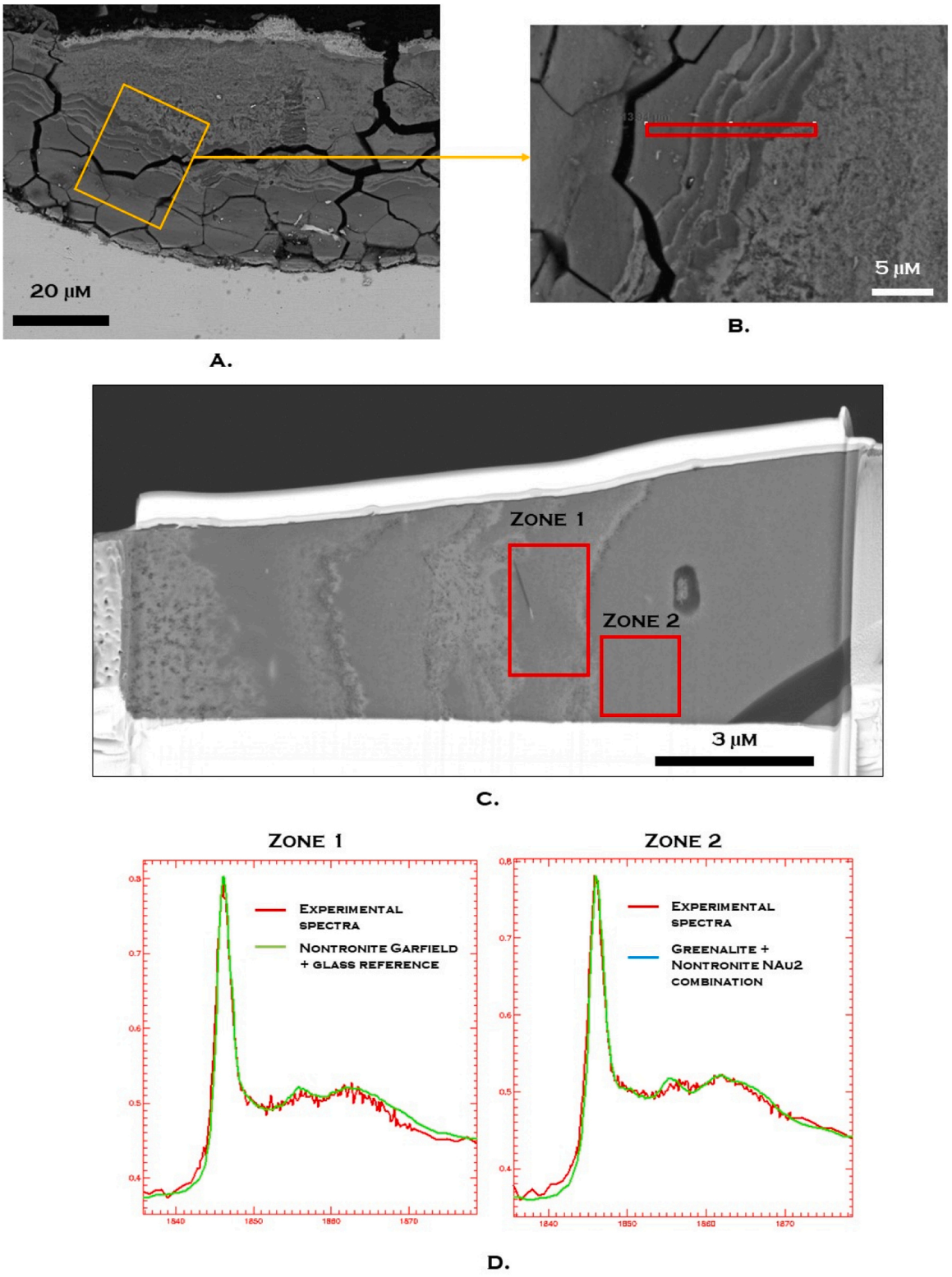

Fig. 15. Sample 2-E, a. SEM-BSE image of the area of interest for STXM characterisation, b. Zoom of the yellow rectangle in a. with the red rectangle the localisation of the thin foil, c. thin foil, d. Spectral signal of zone 1 and 2 and linear combination fit. Zone 1: r^2 = 0.998, chi^2= 0.0210, Zone 2: r^2= 0.988, chi^2=0,0185.

temperature after aging of the cement grout and corrosion tests), were compatible with the dissolution of pyrite and the release of sulphide in solution.

- Romaine *et al.* performed corrosion tests on iron samples in aerated conditions in presence of clay at 80°C. They observed a mix of magnetite and mackinawite in the inner corroded layer. They explained that the presence of iron sulphide was due to the presence of pyrite from the clay without further description of formation mechanism.

Deaerated conditions are too different from the present case and were not considered further in the discussion. Besides, the precipitation

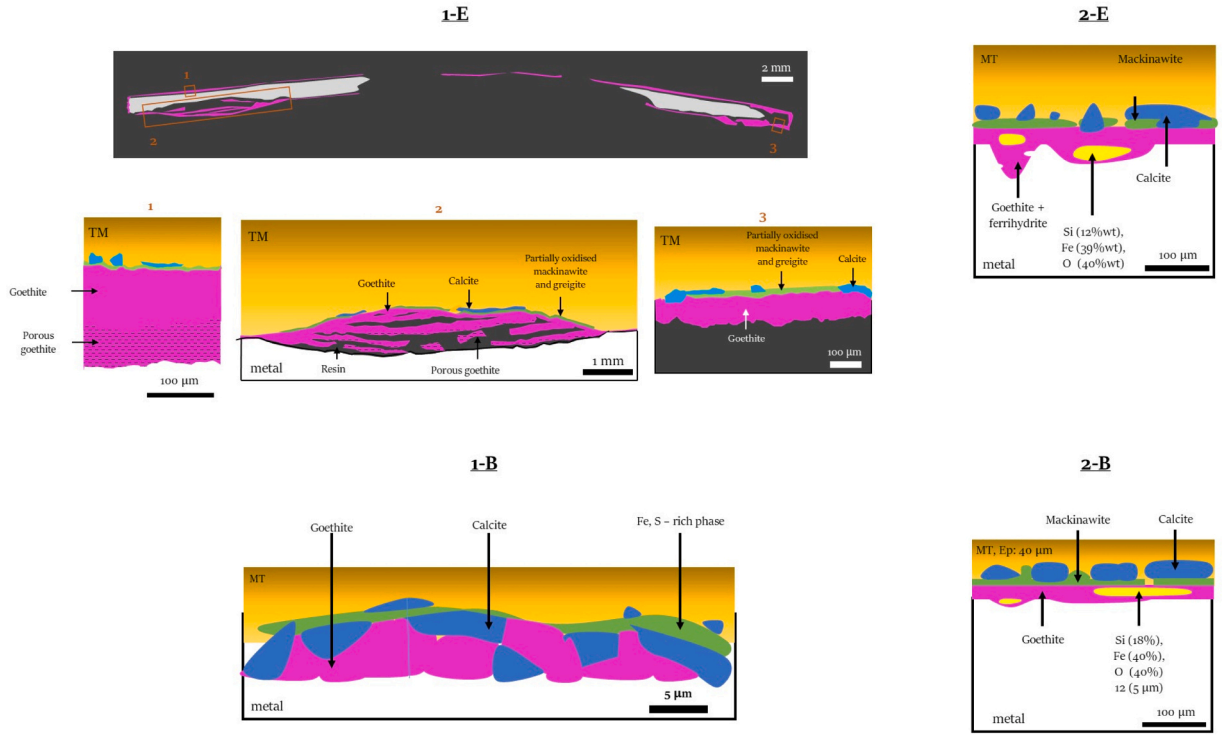

Fig. 16. - Schematics of the corrosion products detected on all four samples.

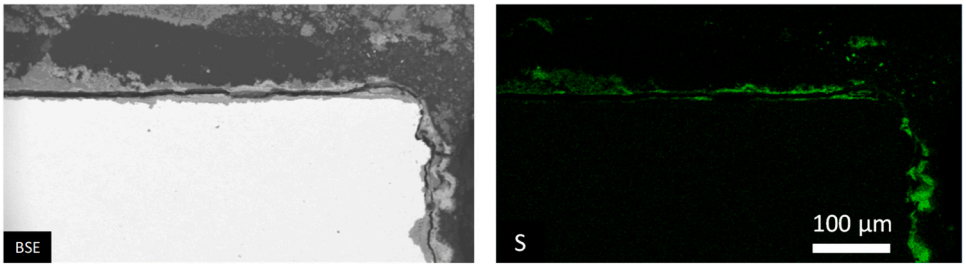

Fig. 17. SEM image (BSE) and sulphur EDX mapping of a corner of sample 1-B.

of sulphide in aerated conditions was observed but not clearly explained in the literature paper reviewed here. A mechanism is proposed here, based on the observations of the samples and on an electrochemical reasoning.

As said before, in the present study, the only possible source of sulphur was the pyrite from the clay. Dissolution/oxidation half equations of the pyrite in an aqueous solution in aerated conditions commonly found in the literature [46,47] lead to the formation of sulphate ions. As reviewed by Chandra et al. [48] O_2 and Fe^{3+} have been recognised as the two most important oxidants. The equations describing the global mechanisms are the following:

$$FeS_2 + \frac{7}{2}O_2 + H_2O \rightarrow Fe^{2+} + 2SO_4^{2-} + 2H^+ \quad (1)$$

$$Fe^{2+} + \frac{1}{4}O_2 + H^+ \rightarrow Fe^{3+} + \frac{1}{2}H_2O \quad (2)$$

$$FeS_2 + 14Fe^{3+} + 8H_2O \rightarrow 15Fe^{2+} + 2SO_4^{2-} + 16H^+ \quad (3)$$

However only iron sulphides were detected in the CP layer. As the environment was aerated, especially at the beginning of the experiment, sulphate reducing bacteria (SRB) were not supposed to be active. The presence of sulphide ions was therefore very probably due to an abiotic process.

An hypothesis could be that the presence of iron sulphide is explained by the fact that the process took place close to the bare metallic surface. This latter imposed locally in the solution a reducing potential. The relationship between $[SO_4^{2-}]$ and [S(-II)] is given by the reaction:

$$SO_4^{2-} + 9H^+ + 8e^- \leftrightarrow HS^- + 4H_2O \quad (4)$$

The redox potential of the couple $(SO_4^{2-})/(HS^-)$ was calculated at 50°C, for a pH range from 7.5 and 8.5, between −0.21 and −0.25 V/ESH based on the thermodynamic approach by Rickard and Luther [49]. While the standard redox potential of the Fe^{2+}/Fe couple calculated at 50°C was −0.45 V/ESH, the following redox reaction could be possible on the metallic surface:

$$SO_4^{2-} + 9H^+ + 4Fe \leftrightarrow HS^- + 4H_2O + 4Fe^{2+} \quad (5)$$

Mackinawite would have then formed following Eq. 6 below.

$$Fe^{2+} + HS^- \leftrightarrow FeS + H^+ \quad (6)$$

When all the pyrite has dissolved the formation of sulphides would stop. Greigite probably formed by the oxidation of mackinawite [32,50].

Fig. 19.a.,b and c. illustrate the first step of the corrosion mechanism involved in the formation of the iron sulphide observed on all four samples.

After this first corrosion step, the corrosion of metallic iron in an aerated aqueous solution continued. This induced the formation of goethite as the main phase precipitating inside the corrosion layer (Fig. 19 d). The formation of the goethite corrosion layer progressed towards the metal under the sulphide layers already formed on the metal surface. This implies that these sulphide layers were permeable to aqueous species.

The corrosion mechanisms were the same for all four samples analysed. However, the nature of the corrosion products was not exactly identical between both stacks. The schematic diagram Fig. 16 underlines the main difference between them: the presence of a poorly crystallised silicon-iron-oxygen rich phase only on the samples of the second stack whatever the vertical position on the latter. These phases were present in the inner part of the corrosion layers, within the goethite showing that they formed after the first goethite precipitation. This disparity between the samples of the two stacks was particularly noteworthy because the sand and claystone (probable sources of Si) used for both stacks have the same origin. As they were both placed in the same container, the temperature and electrolyte concentration were also the same. Such iron silicate phases were observed in deaerated conditions in similar claystone media [20,51]. However, the present experiment was conducted under aerated conditions, which was confirmed by the precipitation of mainly goethite in the corrosion product layers. As it was previously discussed, the claystone of the first stack presented more cracks than the one of the second stack. These cracks ensured a local renewal of the solution at the vicinity of the metallic samples from the outer aerated bulk solution. The samples were therefore maintained in an aerated environment: only goethite was formed. On the contrary when the claystone remained mostly uncracked and compact, as in the second stack, the solution at the vicinity of the samples was not (or less) renewed. This had two consequences. First, the solution was in equilibrium with the claystone which is a source of silicon: the silicon concentration in the solution increased. Second, the oxygen consumed was not renewed which led to the progressive deaeration of the system.

Fig. 18 illustrates, at a fixed potential of 0.2 V, representative of an aerated medium, the thermodynamically predominant phases according to the pH and the silicon concentration in solution. This was obtained by thermodynamic calculations at 50°C. The electrolyte composition was not measured during the corrosion test, however it is considered to be in equilibrium with the Cox-claystone. An electrolyte composition near the one modelled by Andra [52] and corresponding to the equilibrium between the Cox-claystone and the poral water at 50°C was therefore used. Al was added to the composition of the electrolyte in order to allow the formation of the phyllosilicates.

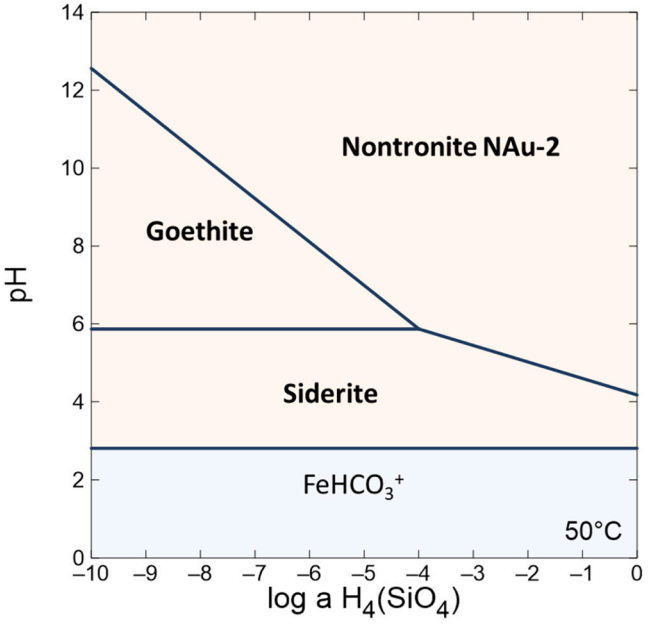

Fig. 18. Predominant phases for varying pH and silicon content at Eh 0.2 V and 50°C, a(Fe) = 0.1 mmol.L^{-1}, a(CO_3^{2-})= 3 mmol.L^{-1}, a(Al^{3+}) =10^{-2} mmol.L^{-1}, a(Mg^{2+}) = 1 mmol.L^{-1}, a(Na^{+}) = 10 mmol.L^{-1}, a(K^{+}) = 1 mmol.L^{-1}, a(Ca^{2+}) = 0.009 mmol.L^{-1}.

This thermodynamic diagram shows that nontronite (that was observed on samples 2-B and 2-E) is predominant for higher concentrations of Si, whatever the pH, could be including the one of the Cox (8.26 at 21°C). Calculations at 20°C show the same thermodynamically stable phases with relatively similar stability domains. This corroborates the hypothesis that the confined system, leading to an increase of the Si concentration in the solution, is responsible for the formation of iron phyllosilicates.

Greenalite is a FeII/FeIII compound and its presence is indicative of much more reducing conditions. This phyllosilicate was only observed experimentally on the bottom sample (2-B). It is possible that anoxic conditions were reached faster for the bottom samples because the oxygen content was already low as it has to diffuse from the surface of the electrolyte. The absence of solution renewal at the vicinity of the metal exacerbated the decrease of oxygen content, allowing greenalite to form.

Both mechanisms (increase of silicon content and decrease of oxygen concentration) could explain the presence of iron phyllosilicates within the goethite layer. At the beginning of the corrosion process the silicon concentration in solution is not sufficient to form nontronite and the oxygen content remains too high to form greenalite: goethite forms. As the equilibrium between the electrolyte and the claystone is achieved, the Si content increases and the oxygen concentration decreases: nontronite and greenalite form in the goethite matrix. It is possible that longer corrosion times could lead to the formation of greenalite on the top samples as well.

Finally, this study confirms that the corrosion processes are highly influenced by the local condition and especially by the difference of compacity of the claystone that can conduct to different renewing of the solution and different aeration. In the particular case of this experimental setup, these phenomena also depend on the distance from the oxygen source (electrolyte/atmosphere interface).

5. Conclusion

The corrosion of two stacks of carbon steel in contact with Cox claystone, immersed in an electrolyte with air cover, for 7 years, including 5 years at 50°C was studied. Several conclusions can be drawn:

- Metal loss and corrosion damage appeared to be mostly present in the top position of the setup and where the surrounding claystone was more cracked and damaged. This was attributed to the proximity with the source of oxygen. The oxygen that diffused from the surface was first consumed by the corrosion of the samples at the top of the stack therefore decreasing the amount of oxygen available to corrode samples in the lower positions. Moreover the cracks in the surrounding claystone caused an easier access to oxygen and possible differential aeration of the system that increased the corrosion phenomenon.
- The corrosion products observed in all samples were mainly composed of goethite. Iron sulphides and calcite were also detected at the former location of the original surface.
- The location of the sulphide layer at the CP/TM interface indicated that it formed at the early beginning of the corrosion process, on the bare metal surface. The origin of the sulphur was the pyrite in the claystone which in the absence of SRB (aerated conditions), is usually said to dissolve into sulphate ions. The formation of sulphide suggested the existence of an abiotic process leading to the reduction of the sulphate ions into sulphide ions at the vicinity of the bare metallic surface imposing a (very)low potential.

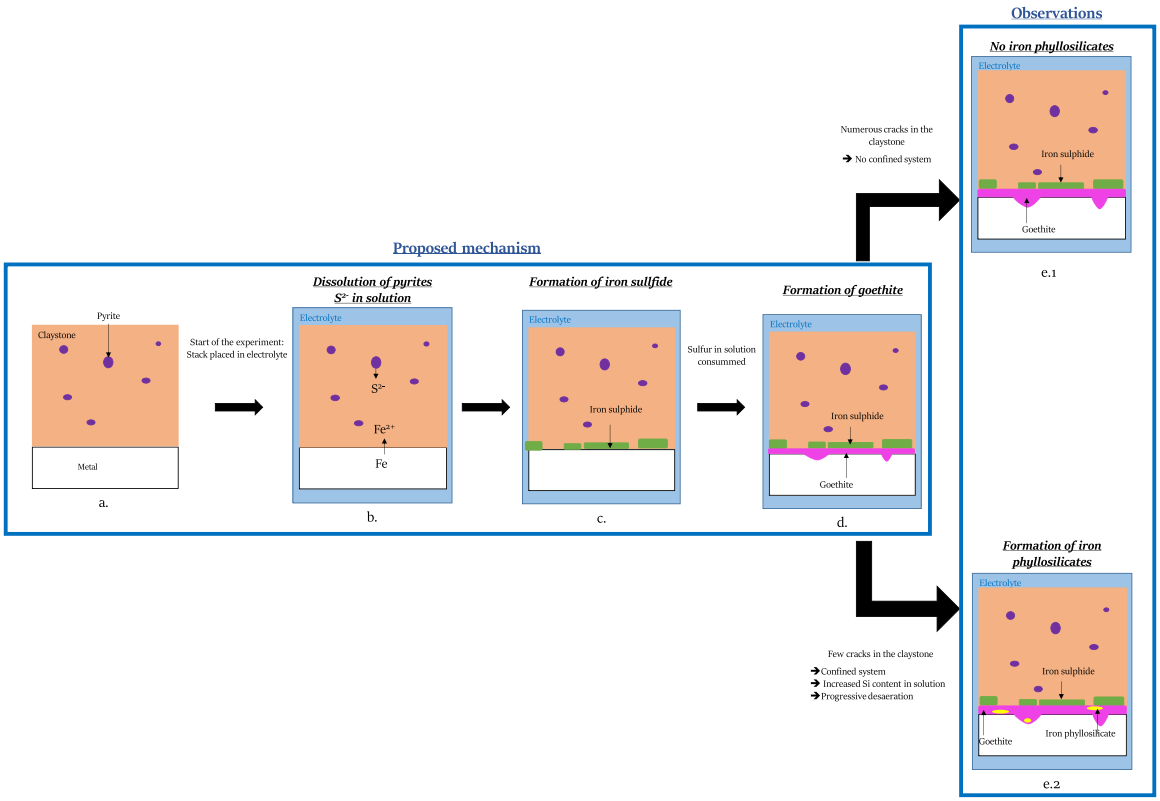

Fig. 19. Proposed mechanism for the corrosion product formation for samples with or without cracking (left rectangle), final observations (right rectangle).

- Despite similar corrosion conditions between both stacks, only the CP observed on the second stack contained iron phyllosilicates which were located within the goethite scale. They were characterised by STXM and identified as a mix of nontronite and greenalite. The different nature of the corrosion products between the two stacks could be due to the difference in the compacity of the claystone. Less cracking resulted in a more confined system which lead to a local increase of the silicate concentration (coming from the clay) in the solution in contact with the claystone as well as to the decrease of the oxygen content (coming from the electrolyte/atmosphere interface) which both allowed the formation of phyllosilicates as suggested by thermodynamic calculations.

This study underlines the influence of the local conditions on the corrosion of the metallic elements in contact with a clay medium. Indeed the compacity of the host rock and the availability of oxygen significantly influences the corrosion mechanisms and evolution, especially during the first aerated stage.

Declaration of Competing Interest

The authors declare that they have no known competing financial interests or personal relationships that could have appeared to influence the work reported in this paper.

Data availability

The data that has been used is confidential.

Acknowledgments

The ISIS4D X-Ray CT platform has been funded by International Campus on Safety and Intermodality in Transportation (CISIT), the Nord-Pas-de-Calais Region, the European Community and the National Center for Scientific Research. The authors gratefully acknowledge the support of these institutions.

This research was funded by ANDRA through the CARABET and CARAMEM 1 and 2 projects.

References

[1] D.G. Bennett, R. Gens, Overview of European concepts for high-level waste and spent fuel disposal with special reference waste container corrosion, J. Nucl. Mater. 379 (2008) 1–8, https://doi.org/10.1016/j.jnucmat.2008.06.001.
[2] ANDRA, Cigéo, (n.d.). https://www.andra.fr/cigeo?gclid=CjwKCAiAyfybBhBKEiwAgtB7fuDdka_Rnw-Tfyzq24ScB1mmmbttgE4nL4LvaZRkFFSULaYpMVhHbhoCflkQAvD_BwE (accessed November 24, 2022).
[3] D. Crusset, V. Deydier, S. Necib, J.-M. Gras, P. Combrade, D. Féron, E. Burger, Corrosion of carbon steel components in the French high-level waste programme: evolution of disposal concept and selection of materials, Corros. Eng. Sci. Technol. 52 (2017) 17–24, https://doi.org/10.1080/1478422X.2017.1344416.
[4] ANDRA, Les recherches de l'ANDRA sur le stockage géologique des déchets radioactifs à haute activité et à vie longue, 2005.
[5] E. Gaucher, C. Robelin, J.M. Matray, G. Négrel, Y. Gros, J.F. Heitz, A. Vinsot, H. Rebours, A. Cassagnabère, A. Bouchet, ANDRA underground research laboratory: interpretation of the mineralogical and geochemical data acquired in the Callovian–Oxfordian formation by investigative drilling, Phys. Chem. Earth Parts A/B/C. 29 (2004) 55–77, https://doi.org/10.1016/j.pce.2003.11.006.
[6] L. de Windt, F. Marsal, J. Corvisier, D. Pellegrini, Modeling of oxygen gas diffusion and consumption during the oxic transient in a disposal cell of radioactive waste, Appl. Geochem. 41 (2014) 115, https://doi.org/10.1016/j.apgeochem.2013.12.005.
[7] C. Yang, J. Samper, J. Molinero, M. Bonilla, Modelling geochemical and microbial consumption of dissolved oxygen after backfilling a high level radiactive waste repository, J. Contam. Hydrol. 93 (2007) 130–148, https://doi.org/10.1016/j.jconhyd.2007.01.008.
[8] F. King, Corrosion of carbon steel under anaerobic conditions in a repository for SF and HLW in Opalinus Clay, 2008.
[9] J.-D. Barnichon, A. Dauzères, L. de Windt, Understanding oxidizing transient conditions in clayey rocks, Appl. Geochem. 98 (2018) 435–447, https://doi.org/10.1016/j.apgeochem.2018.09.018.
[10] Kotelnikova Puigdomenech, Tullborg Pedersen, In-situ determinationof O2 uptake by geological media field data for the redox experiemnt in detailed scale (REX) (2000).
[11] ANDRA, Dossier Argile, 2005.

[12] D. Neff, P. Dillmann, L. Bellot-Gurlet, G. Beranger, Corrosion of iron archaeological artefacts in soil: characterisation of the corrosion system, Corros. Sci. 47 (2005) 515–535, https://doi.org/10.1016/j.corsci.2004.05.029.

[13] A. Gaudin, D. Bartier, L. Truche, E. Tinseau, F. Foct, V. Dyja, A. Maillet, D. Beaufort, First corrosion stages in Tournemire claystone/steel interaction: In situ experiment and modelling approach, Appl. Clay Sci. 83–84 (2013) 457–468, https://doi.org/10.1016/j.clay.2013.06.016.

[14] S. Necib, N. Diomidis, P. Keech, M. Nakayama, Corrosion of carbon steel in clay environments relevant to radioactive waste geological disposals, Mont Terri rock laboratory (Switzerland), Swiss J. Geosci. 110 (2017) 329–342, https://doi.org/10.1007/s00015-016-0259-7.

[15] H. El Hajj, A. Abdelouas, Y. El Mendili, G. Karakurt, B. Grambow, C. Martin, Corrosion of carbon steel under sequential aerobic–anaerobic environmental conditions, Corros. Sci. 76 (2013) 432–440, https://doi.org/10.1016/j.corsci.2013.07.017.

[16] Y.E. Mendili, A. Abdelouas, J.-F. Bardeau, Insight into the mechanism of carbon steel corrosion under aerobic and anaerobic conditions, Phys. Chem. Chem. Phys. 15 (2013) 9197–9204, https://doi.org/10.1039/C3CP50853F.

[17] F.A. Martin, C. Bataillon, M.L. Schlegel, Corrosion of iron and low alloyed steel within a water saturated brick of clay under anaerobic deep geological disposal conditions: an integrated experiment, J. Nucl. Mater. 379 (2008) 80–90, https://doi.org/10.1016/j.jnucmat.2008.06.021.

[18] S. Necib, Y. Linard, D. Crusset, N. Michau, S. Daumas, E. Burger, A. Romaine, M. L. Schlegel, Corrosion at the carbon steel&clay borehole water and gas interfaces at 85°C under anoxic and transient acidic conditions, Corros. Sci. 111 (2016) 242–258, https://doi.org/10.1016/j.corsci.2016.04.039.

[19] S. Necib, M.L. Schlegel, C. Bataillon, S. Daumas, N. Diomidis, P. Keech, D. Crusset, Long-term corrosion behaviour of carbon steel and stainless steel in Opalinus clay: influence of stepwise temperature increase, Corros. Eng. Sci. Technol. 54 (2019) 516–528, https://doi.org/10.1080/1478422X.2019.1621456.

[20] M.L. Schlegel, S. Necib, S. Daumas, M. Labat, C. Blanc, E. Foy, Y. Linard, Corrosion at the carbon steel-clay borehole water interface under anoxic alkaline and fluctuating temperature conditions, Corros. Sci. 136 (2018) 70–90, https://doi.org/10.1016/j.corsci.2018.02.052.

[21] M.L. Schlegel, F. Martin, M. Fenart, C. Blanc, J. Varlet, E. Foy, D. Prêt, N. Trcera, Corrosion at the carbon steel-clay compact interface at 90°C: insight into short- and long-term corrosion aspects, Corros. Sci. 152 (2019) 31–44, https://doi.org/10.1016/j.corsci.2019.01.027.

[22] M. Perronnet, Réactivité des matériaux argileux dans un contexte de corrosion métallique: application au stockage des déchets radioactifs en site argileux, These de doctorat, Vandoeuvre-les-Nancy, INPL, 2004. https://www.theses.fr/2004INPL070N (accessed December 5, 2022).

[23] J. Chen, Contribution à la modélisation de l'endommagement et de la fissure des matériaux cimentaires sous chargement mécanique, corrosion et dessiccation, These de doctorat, Université de Lille (2018-2021), 2021. https://theses.fr/2021LILUN017 (accessed August 31, 2023).

[24] J. Chen, F. Agostini, W. Shen, J. Shao, X. Bourbon, S. Liu, Experimental and numerical studies of a reinforced concrete component subjected to corrosion, Mech. Res. Commun. 129 (2023) 104076, https://doi.org/10.1016/j.mechrescom.2023.104076.

[25] Fiche produit A37, Depery Dufour (n.d.). https://www.depery-dufour.fr/wp-content/uploads/2018/03/A37.pdf (accessed December 8, 2022).

[26] C. Lerouge, S. Grangeon, E.C. Gaucher, C. Tournassat, P. Agrinier, C. Guerrot, D. Widory, C. Fléhoc, G. Wille, C. Ramboz, A. Vinsot, S. Buschaert, Mineralogical and isotopic record of biotic and abiotic diagenesis of the Callovian–Oxfordian clayey formation of Bure (France), Geochim. Cosmochim. Acta 75 (2011) 2633–2663, https://doi.org/10.1016/j.gca.2011.02.025.

[27] F. Agostini, Rapport ANDRA- Démantèlement expérience LAMcube, 2020.

[28] C. Carrière, P. Dillmann, E. Foy, D. Neff, J.J. Dynes, Y. Linard, N. Michau, C. Martin, Use of nanoprobes to identify iron-silicates in a glass/iron/argillite system in deep geological disposal, Corros. Sci. 158 (2019) 108104, https://doi.org/10.1016/j.corsci.2019.108104.

[29] E. Giffaut, M. Grivé, P. Blanc, P. Vieillard, E. Colas, H. Gailhanou, S. Gaboreau, N. C.M. Marty, B. Made, L. Duro, Andra thermodynamic database for performance assessment: ThermoChimie, Appl. Geochem. 49 (2014) 225–236, https://doi.org/10.1016/j.apgeochem.2014.05.007.

[30] Thermo-Chimie (version applicative 4.4.0), (n.d.). https://www.thermochimie-tdb.com/ (accessed August 31, 2023).

[31] P. Blanc, P. Vieillard, H. Gailhanou, S. Gaboreau, N. Marty, F. Claret, B. Madé, E. Giffaut, ThermoChimie database developments in the framework of cement/clay interactions, Appl. Geochem. 55 (2015) 95–107, https://doi.org/10.1016/j.apgeochem.2014.12.006.

[32] Bourdoiseau, Jeannin, Sabot, Rémazeilles, Refait, Characterisation of mackinawite by Raman spectroscopy: Effects of crystallisation, drying and oxidation | Elsevier Enhanced Reader, (n.d.). https://doi.org/10.1016/j.corsci.2008.08.041.

[33] M. Mullet, S. Boursiquot, M. Abdelmoula, J.-M. Génin, J.-J. Ehrhardt, Surface chemistry and structural properties of mackinawite prepared by reaction of sulfide ions with metallic iron, Geochim. Et. Cosmochim. Acta 66 (2002) 829–836, https://doi.org/10.1016/S0016-7037(01)00805-5.

[34] Langumier, Sabot, Obame-Ndong, Jeannin, Sablé, Refait, Formation of Fe(III)-containing mackinawite from hydroxysulphate green rust by sulphate reducing bacteria | Elsevier Enhanced Reader, (n.d.). https://doi.org/10.1016/j.corsci.2009.07.001.

[35] J.-A. Bourdoiseau, M. Jeannin, C. Rémazeilles, R. Sabot, P. Refait, The transformation of mackinawite into greigite studied by Raman spectroscopy, J. Raman Spectrosc. 42 (2011) 496–504, https://doi.org/10.1002/jrs.2729.

[36] C. Remazeilles, A. Dheilly, S. Sable, I. Lanneluc, D. Neff, P. Refait, Microbiologically influenced corrosion process of archaeological iron nails from the sixteenth century, Corros. Eng., Sci. Technol. 45 (2010) 388–394, https://doi.org/10.1179/147842210X12659647007167.

[37] M.L. Schlegel, C. Bataillon, C. Blanc, D. Prêt, E. Foy, Anodic activation of iron corrosion in clay media under water-saturated conditions at 90 °C: characterization of the corrosion interface, Environ. Sci. Technol. 44 (2010) 1503–1508, https://doi.org/10.1021/es9021987.

[38] M.L. Schlegel, C. Bataillon, F. Brucker, C. Blanc, D. Prêt, E. Foy, M. Chorro, Corrosion of metal iron in contact with anoxic clay at 90°C: characterization of the corrosion products after two years of interaction, Appl. Geochem. 51 (2014) 1–14, https://doi.org/10.1016/j.apgeochem.2014.09.002.

[39] W.P. Gates, J.T. Kloprogge, J. Madejova, F. Bergaya, Infrared and Raman spectroscopies of clay minerals, Elsevier, 2017.

[40] M. Ishii, T. Shimanouchi, M. Nakahira, Far infra-red absorption spectra of layer silicates, Inorg. Chim. Acta 1 (1967) 387–392, https://doi.org/10.1016/S0020-1693(00)93207-9.

[41] M. Arab, D. Bougeard, K.S. Smirnov, Experimental and computer simulation study of the vibrational spectra of vermiculite, Phys. Chem. Chem. Phys. 4 (2002) 1957–1963, https://doi.org/10.1039/B110768B.

[42] D. Bard, J. Yarwood, B. Tylee, Asbestos fibre identification by Raman microspectroscopy - Bard - 1997 - Journal of Raman Spectroscopy - Wiley Online Library, Journal or Raman Spectroscopy (1998). https://analyticalsciencejournals.onlinelibrary.wiley.com/doi/abs/10.1002/%28SICI%291097-4555%28199710%2928%3A10%3C803%3A%3AAID-JRS151%3E3.0.CO%3B2-7 (accessed April 23, 2023).

[43] A. Wiewióra, T. Więckowski, A. Sokołowska, The Raman spectra of kaolinite sub-group minerals and of pyrophyllite, in: 1979. https://www.semanticscholar.org/paper/The-Raman-spectra-of-kaolinite-sub-group-minerals-Wiewi%C3%B3ra-Wi%C8%A9ckowski/7afeb368bad07af79e8ef588e8c480634c10719e (accessed April 23, 2023).

[44] D. Tromans, Temperature and pressure dependent solubility of oxygen in water: a thermodynamic analysis, Hydrometallurgy 48 (1998) 327–342, https://doi.org/10.1016/S0304-386X(98)00007-3.

[45] M. Robineau, R. Sabot, M. Jeannin, V. Deydier, D. Crusset, P. Refait, Mechanisms of localized corrosion of carbon steel associated with magnetite/mackinawite layers in a cement grout, Mater. Corros. 72 (2021) 194–210, https://doi.org/10.1002/maco.202011696.

[46] E. Ahlberg, K.S.E. Forssberg, X. Wang, The surface oxidation of pyrite in alkaline solution, J. Appl. Electrochem 20 (1990) 1033–1039, https://doi.org/10.1007/BF01019585.

[47] I.C. Hamilton, R. Woods, An investigation of surface oxidation of pyrite and pyrrhotite by linear potential sweep voltammetry, J. Electroanal. Chem. Interfacial Electrochem. 118 (1981) 327–343, https://doi.org/10.1016/S0022-0728(81)80551-7.

[48] A.P. Chandra, A.R. Gerson, The mechanisms of pyrite oxidation and leaching: a fundamental perspective, Surf. Sci. Rep. 65 (2010) 293–315, https://doi.org/10.1016/j.surfrep.2010.08.003.

[49] D. Rickard, G.W. Luther, Chemistry of iron sulfides, Chem. Rev. 107 (2007) 514–562, https://doi.org/10.1021/cr0503658.

[50] S. Boursiquot, M. Mullet, M. Abdelmoula, J.-M. Génin, J.-J. Ehrhardt, The dry oxidation of tetragonal FeS1-xmackinawite, Phys. Chem. Min. 28 (2001) 600–611, https://doi.org/10.1007/s002690100193.

[51] M.L. Schlegel, S. Necib, S. Daumas, C. Blanc, E. Foy, N. Trcera, A. Romaine, Microstructural characterization of carbon steel corrosion in clay borehole water under anoxic and transient acidic conditions, Corros. Sci. 109 (2016) 126–144, https://doi.org/10.1016/j.corsci.2016.03.022.

[52] T.De Echave, Etude des mécanismes d'altération des verres nucléaires sous radiolyse alpha et en conditions environnementales, These de doctorat, Montpellier, 2018. https://theses.fr/2018MONTS051 (accessed December 21, 2022).